



# In-situ construction of coral-like porous P-doped g-C<sub>3</sub>N<sub>4</sub> tubes with hybrid 1D/2D architecture and high efficient photocatalytic hydrogen evolution

Mao Wu<sup>a</sup>, Jin Zhang<sup>a</sup>, Bei-bei He<sup>a</sup>, Huan-wen Wang<sup>a</sup>, Rui Wang<sup>a,\*</sup>, Yan-sheng Gong<sup>a,b,\*</sup>

<sup>a</sup> Faculty of Materials Science and Chemistry, China University of Geosciences, Wuhan 430074, PR China

<sup>b</sup> Engineering Research Center of Nano-Geomaterials of Ministry of Education, China University of Geosciences, 388 Lumo Road, Wuhan 430074, PR China

## ARTICLE INFO

### Keywords:

Tubular g-C<sub>3</sub>N<sub>4</sub>  
1D/2D heterojunction  
Photocatalytic hydrogen evolution  
Phosphorus doping

## ABSTRACT

Developing novel methods to prepare hollow one-dimensional (1D) carbon nitride (g-C<sub>3</sub>N<sub>4</sub>) nanostructure is highly attractive in photocatalytic water splitting for hydrogen production. Herein, a simple, self-assembly synthesis of coral-like 3D porous P-doped g-C<sub>3</sub>N<sub>4</sub> tubes (PCNT) by the combination of pyrolysis and freeze-drying method was reported. Attributed to the integrated merits of 1D tubular structure, 2D nanosheets and phosphorus doping, the as-prepared hollow PCNT exhibits superior photocatalytic activity under visible light irradiation. Owing to their higher specific surface area, enhanced light absorption, and better charge carrier separation and transfer, the maximum apparent photocatalytic hydrogen evolution rate of PCNT is 2020 μmol g<sup>-1</sup> h<sup>-1</sup>, which is about 4.7 folds and 22.4 folds than that of g-C<sub>3</sub>N<sub>4</sub> tubes and pristine bulk g-C<sub>3</sub>N<sub>4</sub>, respectively. Moreover, a possible photocatalytic mechanism and nanostructure formation process based on the experimental results are proposed. The novel growth strategy developed here may offer a new avenue for the rational design and synthesis of potentially efficient photocatalyst with 1D/2D integrated nanoarchitecture.

## 1. Introduction

Clean hydrogen generation through photocatalytic water splitting from inexhaustible solar energy has been attracted worldwide scientific interest to address the global energy crisis and environmental problems [1–3]. Due to its narrow indirect band gap ( $E = 2.7$  eV) and high chemical stability, metal-free polymeric graphite-like carbon nitride (usually denoted as g-C<sub>3</sub>N<sub>4</sub>) has been received intensive research since it was firstly discovered to be used as a photocatalyst for hydrogen production by Wang et al. [4–7]. However, the pristine g-C<sub>3</sub>N<sub>4</sub> only shows a moderate photocatalytic activity owing to its insufficient visible-light utilization efficiency, fast recombination of photo-generated electron-holes, and relative low surface area [8,9]. Although various modification strategies are adopted to overcome these deficiencies, such as heteroatom doping with non-metal (e.g., S, P) [10,11] or metal (e.g., Fe, Ni) atoms [12,13], loading noble metal (like Pt, Au, and Pd) on the surface [14–16], construction of heterojunctions with other semiconductors [17,18], as well as exfoliating it into two-dimensional (2D) nanosheets [19–21]. Unfortunately, the photocatalytic efficiency of these g-C<sub>3</sub>N<sub>4</sub>-based photocatalysts is still far from satisfactory. Therefore, some synergetic strategies, including the preparation of element doped porous g-C<sub>3</sub>N<sub>4</sub>, introducing defects to g-C<sub>3</sub>N<sub>4</sub>

nanosheets, as well as morphology and structure adjustment, were applied to further enhance its photocatalytic activity [22–25].

Morphology and structure adjustment have been considered as an efficient way to enhance the photocatalytic quantum efficiency of g-C<sub>3</sub>N<sub>4</sub>. The active site of g-C<sub>3</sub>N<sub>4</sub> is enhanced by constructing various morphologies including nanotubes, hollow spheres, nanofibers, and bivalve structures [26]. Tubular nanostructure with open mesoporous morphology can efficiently transfer the photogenerated carriers along the 1D path, which possess direct and rapid electronic transport pathway, excellent optical properties, and high surface photocatalytic efficiency [27,28]. Very recently, one-dimensional g-C<sub>3</sub>N<sub>4</sub> materials have been synthesized by hard/soft template routes, self-assembly, and liquid-phase reactions [29–32]. For instance, hexagonal g-C<sub>3</sub>N<sub>4</sub> tubular structure was fabricated by Fu et al. through phosphorous acid-assisted hydro-thermal method [33]. Phosphorus-doped g-C<sub>3</sub>N<sub>4</sub> nanotubes were synthesized through a thermal reaction of melamine and sodium hypophosphite monohydrate [34]. Defect-engineered g-C<sub>3</sub>N<sub>4</sub> nanotubes were also obtained by self-assembled approach [35]. However, the methods mentioned above have drawbacks related to the harsh synthetic procedures, operational complexity, and the use of hazardous reagents, which limit the large-scale preparation of g-C<sub>3</sub>N<sub>4</sub> nanotubes. Thus, it is highly desirable to develop a facile, low-cost, and sustainable

\* Corresponding author at: Faculty of Materials Science and Chemistry, China University of Geosciences, Wuhan, 430074, PR China.

\*\* Corresponding author.

E-mail addresses: [wangrui@cug.edu.cn](mailto:wangrui@cug.edu.cn) (R. Wang), [gongysh@cug.edu.cn](mailto:gongysh@cug.edu.cn) (Y.-s. Gong).

<https://doi.org/10.1016/j.apcatb.2018.09.037>

Received 31 July 2018; Received in revised form 9 September 2018; Accepted 11 September 2018

Available online 12 September 2018

0926-3373/ © 2018 Elsevier B.V. All rights reserved.

routes to prepare orderly g-C<sub>3</sub>N<sub>4</sub> nanotubes with hierarchical structure.

Although the high specific surface area and distinct morphology of 2D g-C<sub>3</sub>N<sub>4</sub> nanosheets, which have been obtained by thermal exfoliation and liquid-exfoliation in hazardous reagents [31,34], are responsible for their enhanced photocatalytic activity, the uncontrolled aggregation problems and the largely increased band gap of 2D g-C<sub>3</sub>N<sub>4</sub> nanosheets caused by the strong quantum confinement effects (QCE) and decrease of conjugation length inhibit their practical application for solar energy conversion [36]. Interconnecting the individual g-C<sub>3</sub>N<sub>4</sub> nanosheets into another nanoarchitectures (e.g. nanotube and nanospheres) can effectively avoid the agglomeration of nanosheets [24]. However, few studies have been concerned about this issue.

On the other hand, as a heteroatom doping strategy, the existence of phosphorus in g-C<sub>3</sub>N<sub>4</sub> can tune the band gap structure and extend the light absorption, thus increasing the separation efficiency of photo-generated electrons and holes, creating more active sites, and benefiting the photocatalytic activity [37]. Up to date, phosphorus doped (P-doped) 2D g-C<sub>3</sub>N<sub>4</sub> nanosheets and g-C<sub>3</sub>N<sub>4</sub> nanotube have both been separately aroused much attention, for example, Qiao et al. [36] reported that P-doped g-C<sub>3</sub>N<sub>4</sub> exhibited a high visible-light photocatalytic H<sub>2</sub>-production activity of 1596  $\mu\text{mol g}^{-1} \text{h}^{-1}$  and an apparent quantum efficiency of 3.56% at 420 nm. Jiang et al. [38] fabricated P-doped tubular g-C<sub>3</sub>N<sub>4</sub> under a sodium pyrophosphate-assisted hydrothermal process, showing a higher hydrogen evolution rate than that of bulk g-C<sub>3</sub>N<sub>4</sub>. However, to the best of our knowledge, the simultaneous combination g-C<sub>3</sub>N<sub>4</sub> nanotube, 2D nanosheets and phosphorus doping have not been reported yet. It can be anticipated that this ternary architecture would integrate the above-mentioned merits of 1D tubular structure and porous P-C<sub>3</sub>N<sub>4</sub> ultrathin nanosheets collectively.

Inspired by the above investigations, coral-like 3D porous P-doped g-C<sub>3</sub>N<sub>4</sub> tubes (PCNT) were designed and prepared by a simple combination of pyrolysis and freeze-drying method in this study. Thanks to the advantages of the formation of the heterojunction structure, large specific surface area for the integration of 2D nanosheets on g-C<sub>3</sub>N<sub>4</sub> tubes, and enhanced visible-light absorption by phosphorus doping, the as-synthesized PCNT exhibits a dramatically enhanced visible-light photocatalytic H<sub>2</sub> production rate and robust reliability. The formation mechanism of coral-like 3D porous g-C<sub>3</sub>N<sub>4</sub> tubes structure and the reasons for the improved photocatalytic performance of PCNT were finally proposed based on the experimental results.

## 2. Experimental section

### 2.1. Raw materials

All the reagents were analytic pure and used without further purification. Dicyandiamide (A.R.  $\geq 98\%$ ) and phytic acid (10%) were purchased from Aladin corporation. Deionized water was used in all the experiments.

### 2.2. Preparation of the bulk g-C<sub>3</sub>N<sub>4</sub>

Bulk g-C<sub>3</sub>N<sub>4</sub> was prepared by a conventional method with a minor revision. In brief, 2 g dicyandiamide (DCDA) was placed in the crucible with a cover and heated at 600 °C for 4 h with a ramping rate of 2 °C/min. After that, the product was milled into fine powder after cooling to room temperature naturally to get the final bulk g-C<sub>3</sub>N<sub>4</sub> samples.

### 2.3. Preparation of 3D porous P-doped carbon nitride tube

First, 2 g dicyandiamide and 4 mL phytic acid (PA) solution were added into 50 mL water under constant stirring for 30 min, then the mixture was transferred into a 100 mL Teflon-lined stainless autoclave and kept at 180 °C for 4 h. Second, after cooling to room temperature naturally, the hydrothermal-treated dicyandiamide (HTD) was poured into liquid nitrogen quickly to freeze it. To obtain the solid

composition, a freeze-dried method was used and maintained for 24 h. Last, the dried white powder was wrapped by aluminum foil and heated to 600 °C for 4 h with a ramping rate of 2 °C/min in a muffle furnace. For comparison, the photocatalysts with different ratios of phytic acid to DCDA were prepared and denoted as PCNT-*x* (*x* = 1,2,3,4, representing the volume of phytic acid solution) except that the sample containing no phytic acid was named as TCN.

### 2.4. Characterization

The crystal structures were carried out by X-ray diffraction (XRD) (D8-FOCUS, BrukerAXS, Panalytical) using Cu K $\alpha$  radiation. Fourier transform infrared (FTIR, Perkin-Elmer, USA) was used to obtain the function groups. The chemical status was determined by XPS using a VG Scientific ESCALAB Mark II spectrometer equipped (Escalab 250XI, ThermoFisher) with two ultrahigh vacuum (UHV) chambers. Scanning electronic microscopy (SEM, S4800, Japan) and transmission electron microscope (TEM, TF20, FEI) were used to observe the morphology and composition structure. The N<sub>2</sub> adsorption/desorption analysis was conducted by Micromeritics ASAP2460 surface area analyzer at 77 K. Optical absorbance spectra were obtained using a UV-vis diffuse reflectance spectrometer (Lambda35, Perkin Elemer) with BaSO<sub>4</sub> as the reflectance standard. The PL spectra and time-resolved PL spectra were obtained using an Edinburgh FLS980 spectrophotometer (PANalytical, Axios) at an excitation wavelength of 340 nm.

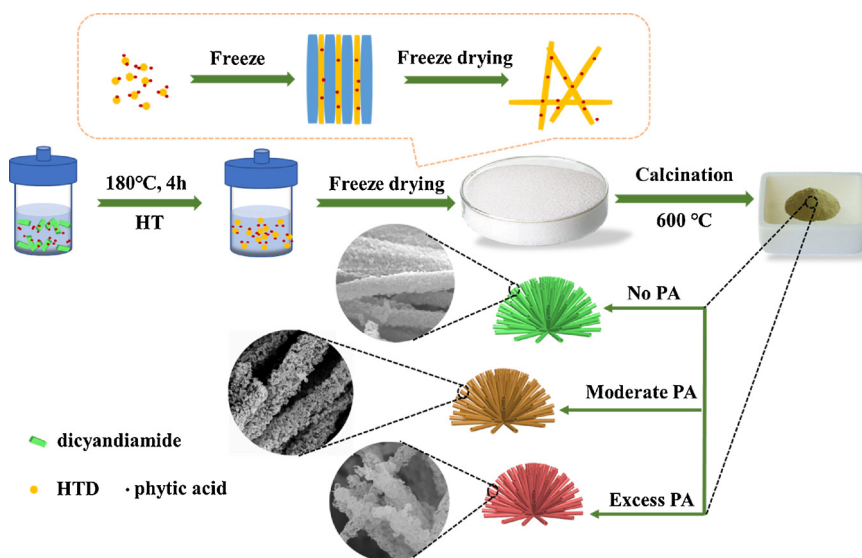
### 2.5. Photocatalytic activity measurement

Photocatalytic hydrogen production experiments were accomplished in a 300 mL closed Pyrex reactor with a quartz window at a constant temperature of 10 °C. A 300 W Xe-lamp (CEL-HXF300, Au-Light, China) with a cutoff ( $\lambda \geq 420 \text{ nm}$ ) was used as the light source. In all the tests, 50 mg photocatalyst was dispersed in 100 mL solution containing 10 vol% triethanolamine (TEOA), and 3 wt% Pt was loaded on the surface of catalyst by the conventional photo-deposited method using H<sub>2</sub>PtCl<sub>6</sub>·6H<sub>2</sub>O. Prior to the reaction, the reactor was bubbled with N<sub>2</sub> for 30 min to remove air. Photocatalytic H<sub>2</sub> evolution was then initiated by irradiating the suspension at a light intensity of about 33.8 mW·cm<sup>-2</sup>. The gaseous product was analyzed by gas chromatography (GC-2014, SHIMADZU, Japan) with a TCD detector using N<sub>2</sub> as the carrier gas. The cycling experiment was performed by bubbling with N<sub>2</sub> to refresh the reaction system. To evaluate the apparent quantum efficiency (AQE) of the photocatalyst, a series of optical filters (420 nm, 450 nm and 500 nm) was used. For the quantum efficiency at 420 nm, the intensity of irradiation was controlled to about 4.1 mW·cm<sup>-2</sup>. While at 450 nm and 500 nm, the irradiation area was fixed at 38.5 cm<sup>2</sup> and the intensity was 3.5 mW·cm<sup>-2</sup> and 4.3 mW·cm<sup>-2</sup> respectively. The apparent quantum efficiency was calculated using the following Eq. (1):

$$\text{AQE} = \frac{2 \times \text{number of hydrogen molecules}}{\text{number of incident photon}} \times 100\% \quad (1)$$

### 2.6. Photoelectrochemical measurements

Photochemical tests were performed using a CHI660D electrochemical workstation (Chenhua Instruments Co. Shanghai) in a typical three-electrode system with 0.5 M Na<sub>2</sub>SO<sub>4</sub> aqueous solution electrolyte. The Pt wire was used as a counter electrode and Ag/AgCl electrode as a reference electrode, while the samples loaded on the FTO were served as the working electrodes. The slurry of sample on the FTO was prepared as follows: 5 mg of photocatalyst were added into the mixed solution consisting of 10  $\mu\text{L}$  of Nafion solution (5 wt%), 100  $\mu\text{L}$  isopropanol and 300  $\mu\text{L}$  water. After ultrasonic treatment for 60 min, the resultant catalyst slurry was spread on the FTO glass with an area of  $\sim 1 \text{ cm}^2$  and then dried in air. Electrochemical impedance spectroscopy



**Scheme 1.** Schematic illustration for the formation of 3D porous P-doped carbon nitride tubes.

(EIS) was recorded at an applied potential of 0.01 V versus SCE over the frequency range from 1 MHz to 0.1 Hz.

### 3. Results and discussion

Coral-like 3D porous P-doped carbon nitride tubes were prepared by pyrolysis and freeze-drying method, the detailed process was explicated in [Scheme 1](#).

Here, dicyandiamide was chosen as the precursor of carbon nitride, mainly due to that it could dissolve in water to form homogeneous solution after the hydrothermal treatment, and its chemical composite would change into the compound containing oxygen, thus could be doped oxygen into carbon nitride via calcination. Phytic acid not only acted as the source of phosphorus, but also played an important role in the formation of porous external framework. The procedure could be split into three sections as shown in the experimental details. Compared with dicyandiamide (DCD), HTD (hydrothermally treated dicyandiamide) samples presented different XRD pattern (Fig. S1), which was in accordance with the previous report [19]. What's more, the precursor of TCN and PCNT-3 had the same XRD pattern, indicating that there was no change for HTD solution after the addition of phytic acid.

Scanning electron microscopy (SEM) was used to observe the morphology and composition structure of the as-prepared photocatalysts. As shown in Fig. 1a, the carbon nitride prepared by freeze-drying method exhibited a coral-like structure with many antennas, which was

much different from those bulk g-C<sub>3</sub>N<sub>4</sub>. Furthermore, the antenna consisted of hollow tube with a diameter of 1–3 μm (Fig. 1e), which enhanced the specific surface areas and electron transport, thus making more exposed active edges and efficient electron-hole separation than that of bulk g-C<sub>3</sub>N<sub>4</sub> [35]. Fig. 1b, c, d showed the morphology of P-doped carbon nitride with different ratio of phytic acid, all the samples retained uniform tubular structure (Figs. 1f, g, h and S2) with different microstructure. The PCNT-1 sample with less phytic acid was loaded with massive thin sheets. With increasing phytic acid ratio, these nanosheets changed into hollow flower buds, and distributed uniformly on the surface of the tubes. When the molar ratio of phytic acid was excessive, the tubes were absolutely constituted with pieces of nanosheets, and the space between them was commodious. So the phytic acid played an important role in the microstructure adjustment of g-C<sub>3</sub>N<sub>4</sub> tubes (Scheme 1).

To further figure out the internal structure of PCNT-3 sample, transmission electron microscope (TEM) measurement was carried out, and the results were depicted in Fig. 2a. It was further confirmed that the tubular structure was hollow and the tube wall was made up of flower buds-like carbon nitride, which was in accordance with the above SEM images. What's more, these flower buds were also hollow with about 18 nm thick shell (Fig. 2d), just like dozens of single graphitic carbon nitride layers growing up crisscrossing one by one (Fig. 2b and c), thus enhancing the interaction and efficiency of electron-hole separation [40]. The inset in Fig. 2d showed a selected area electron

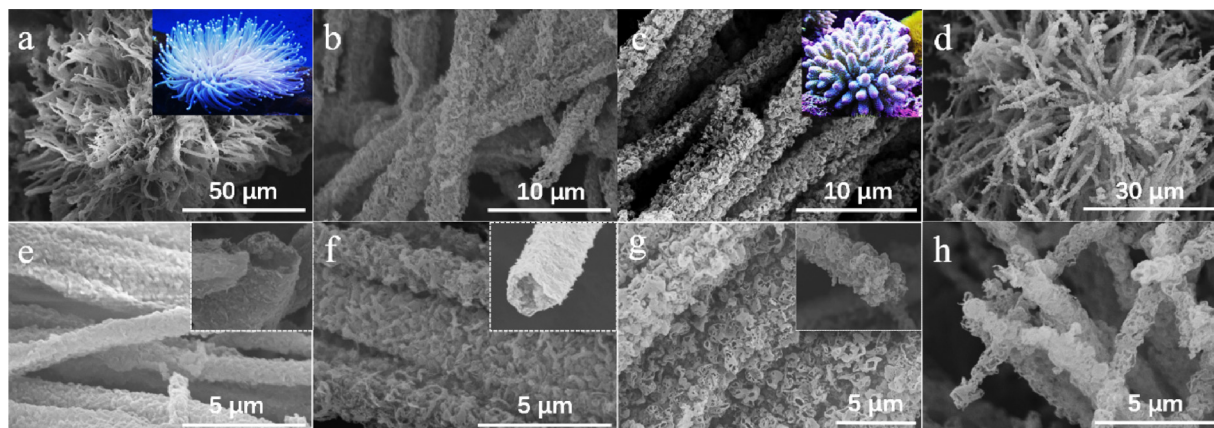


**Fig. 1.** Typical SEM images of (a, e) TCN, (b, f) PCNT-1, (c, g) PCNT-3 and (d, h) PCNT-4 samples.



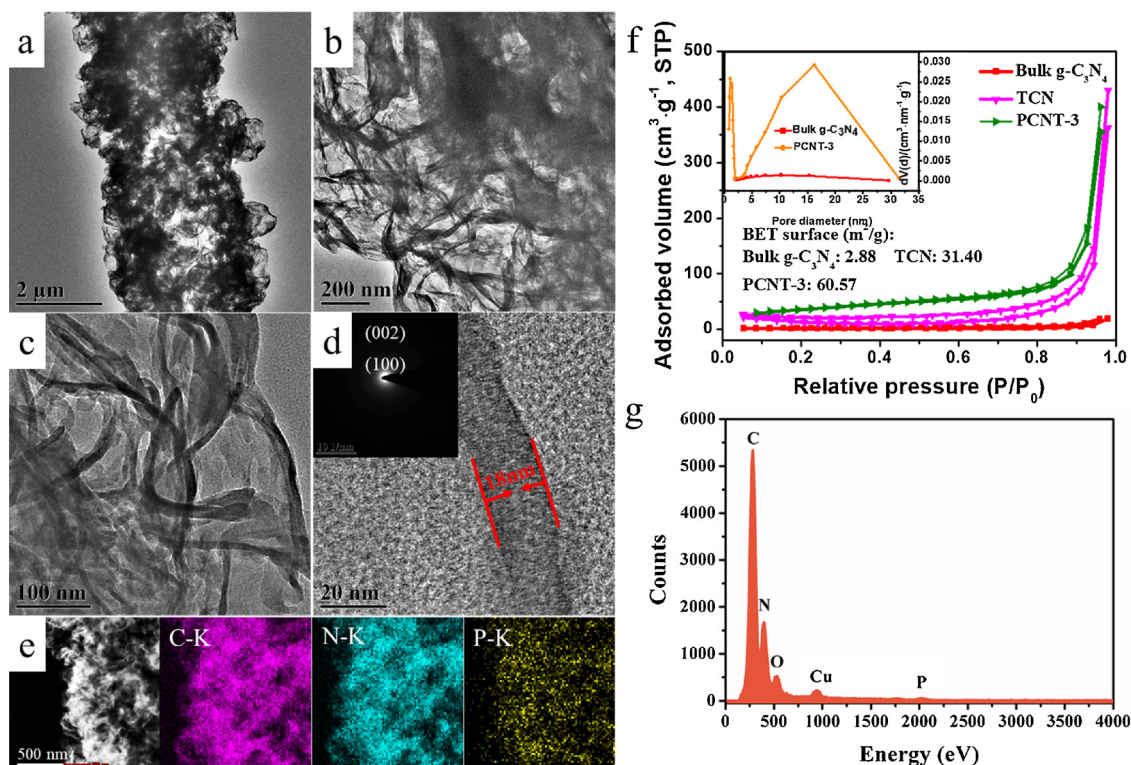


Fig. 2. (a, b, c, d) TEM images and SAED pattern of PCNT-3 sample (inset); (e) Corresponding elemental mapping of C, N, P elements; (f) Nitrogen adsorption-desorption isotherm and the pore size distribution (inset) of bulk g-C<sub>3</sub>N<sub>4</sub>, TCN and PCNT-3 samples; (g) EDX results of PCNT-3 sample.

diffraction (SAED) pattern of the PCNT-3 sample, there were two diffraction rings related to the (002) and (100) planes of g-C<sub>3</sub>N<sub>4</sub>, suggesting their polycrystalline nature [22]. In order to investigate the porous multilevel structure, N<sub>2</sub> adsorption/desorption analysis was used to show its BET surface area and pore information. As shown in Fig. 2f, all of the N<sub>2</sub> isotherms performed type IV isotherms, indicating that the samples were mesoporous with the surface area of 2.88 m<sup>2</sup>/g (bulk g-C<sub>3</sub>N<sub>4</sub>), 31.4 m<sup>2</sup>/g (TCN) and 60.57 m<sup>2</sup>/g (PCNT-3), respectively. It was obvious that PCNT-3 sample owned higher BET surface areas, exhibiting about 21 times larger than that of bulk g-C<sub>3</sub>N<sub>4</sub> and 1.9 times than TCN (Fig. S4, Table S1). Meanwhile, the main concentration of its pore diameter was at 1.2 nm and 16.3 nm, which further confirmed the porous structure on the surface of the tube in SEM and TEM images (Figs. 1, 2a-c). In Fig. 2g, the EDX results confirmed the existence of P element in the composition, illustrating that P element was successfully doped. At the same time, C, N and P three major elements mapping was also performed to present the distribution. As shown in Fig. 2e, all of them were distributed uniformly on the surface of the tubes.

Fig. 3a showed the typical XRD patterns of bulk g-C<sub>3</sub>N<sub>4</sub>, TCN and

PCNT-3 samples. In the case of bulk g-C<sub>3</sub>N<sub>4</sub>, there were two characteristic peaks at  $2\theta = 13.1^\circ$  and  $27.5^\circ$ , belonging to the (100) and (002) diffraction planes, which was related to the in-plane tri-s-triazine motif and the interlayer stacking reflection of conjugated aromatic segments [39]. While the XRD pattern of TCN showed only an overt peak at  $2\theta = 27.9^\circ$ , larger than bulk g-C<sub>3</sub>N<sub>4</sub>, indicating the decrease of stacking distance [34,39]. Meanwhile, the peak intensity displayed a palpable weak tendency, which might be ascribed to the poorer in-planar periodicity and was accordant with other reports about carbon nitride tubes [31–35]. After the phosphorus element was doped into it, the peak at  $27.9^\circ$  shifted to  $27.8^\circ$ , suggesting that the distance of in-planar nitride pores increased. This was because P atom replaced C atom and P atom had a bigger radius than C atom [21]. As for its slight stronger peak intensity than TCN, it could be seen from the SEM pictures that parts of tubular structure turned into nanosheets after P-doping, so the ratio of tubes would decrease with increasing P content, thus followed by the promotion of peak intensity. The FT-IR patterns of bulk g-C<sub>3</sub>N<sub>4</sub>, TCN and PCNT-3 were displayed in Fig. 3b. All the IR absorption bands were similar. The peaks ranging from 3000 cm<sup>-1</sup> to

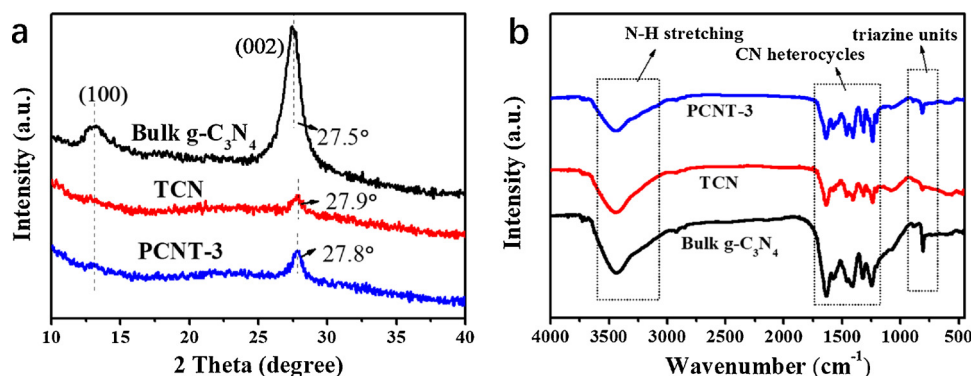


Fig. 3. (a) XRD patterns and (b) FTIR spectra of bulk g-C<sub>3</sub>N<sub>4</sub>, TCN and PCNT-3 samples.

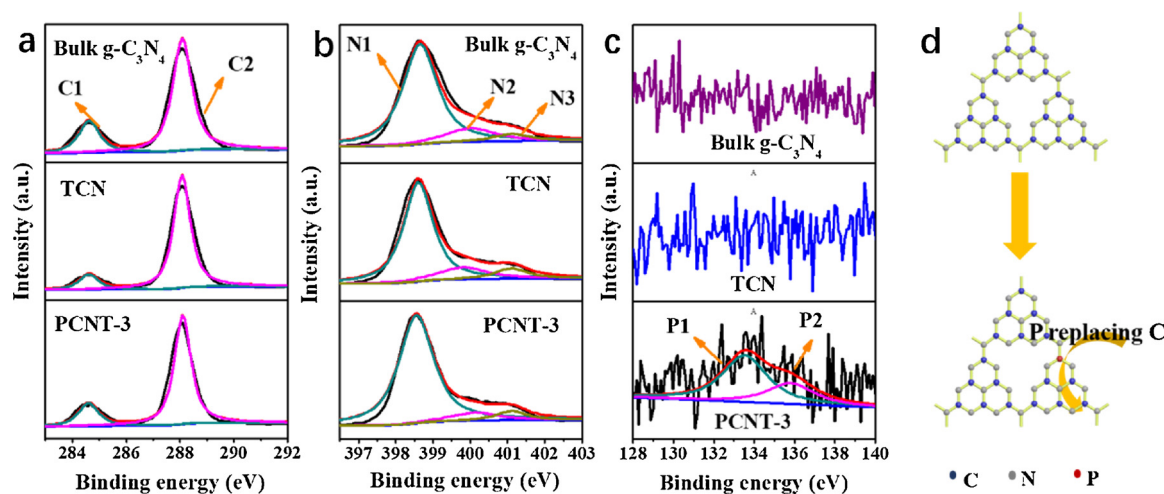


Fig. 4. XPS spectra of (a) C 1 s, (b) N 1 s, (c) P 2 p for bulk g-C<sub>3</sub>N<sub>4</sub>, TCN and PCNT-3 samples; (d) Schematic structure of P-doped g-C<sub>3</sub>N<sub>4</sub> tube.

3600 cm<sup>-1</sup> were due to the O–H and N–H stretching vibration modes, while the peaks between 1200 cm<sup>-1</sup> and 1600 cm<sup>-1</sup> were the stretching vibration modes of CN heterocycles. The sharp peak at 800 cm<sup>-1</sup> was attributed to the tri-s-triazine units [28]. However, the intensities of the CN heterocycles and tri-s-triazine units in PCNT-3 were lower than that of other samples, indicating the loss of nitrogen element in these groups. Notably, there were no P-related groups, which might be due to the low content of phosphorus.

Moreover, XPS was carried out to verify the composition and chemical status of the PCNT-3 (Fig. 4). As shown in Fig. 4a and b, these three samples owned similar XPS spectra of C 1 s and N 1 s. The C 1 s spectra could be resolved into two main peaks: C1 (284.8 eV), C2 (288.2 eV), which were assigned to graphitic C–C and the carbon atom in the N=C(–N)<sub>2</sub> group of g-C<sub>3</sub>N<sub>4</sub>. For N 1 s spectra, there were three peaks at 398.9 eV (N1), 399.9 eV (N2) and 401.1 eV (N3), the peak at 398.9 eV was attributed to C=N–C, the peak at 399.9 eV was the tertiary N bonded to carbon atoms, and the last peak at 401.1 eV was corresponded to C–NH<sub>2</sub>. In Fig. 4c, there was no intensity signal of P 2 p for both bulk g-C<sub>3</sub>N<sub>4</sub> and TCN, while PCNT-3 showed two P-related peaks at 136.1 eV (P2) and 133.8 eV (P1), assigned to P–O and P–N, indicating that P was successfully doped and replaced C in triazine rings [33]. By analyzing the external elements content (Table S2), PCNT-3 contained 0.87 wt.% phosphorus, and the ratio between C atom and N atom was 0.866, higher than that of bulk g-C<sub>3</sub>N<sub>4</sub> (0.700) and TCN (0.795). The results could be explicated from two major sides: First, during the hydrothermal reaction, there were a small amount of ammonia escaping, leading to the decrease of N concentration. Second, phytic acid might contribute a part of C element to it.

To study the optical properties and electronic band structure of bulk g-C<sub>3</sub>N<sub>4</sub>, TCN and PCNT-3, UV–vis spectra and valence band XPS spectra were characterized. From Fig. 5a, it can be seen that bulk g-C<sub>3</sub>N<sub>4</sub> had stronger absorption than TCN in visible light region and PCNT-3 within 450 nm. However, at the wavelength longer than 450 nm, the absorbance of PCNT-3 was the highest owing to its multiple reflection caused by porous structure and P-doping function of broadening absorption tail. In addition, the color of PCNT-x became red with increasing phytic acid (Fig. S3). The bandgaps of bulk g-C<sub>3</sub>N<sub>4</sub>, TCN and PCNT-3, obtained by the Kubelk-Munk method were 2.52 eV, 2.67 eV and 2.58 eV, respectively (Fig. 5b). The PCNT-3 sample possessed narrower bandgap than TCN, resulting in more photogenerated electrons under visible light. Combining the VB XPS spectra (Fig. 5c), the location of VB and CB band was displayed in Fig. 5d. The CB position of PCNT-3 (–0.33 eV) got rise to negative shift compared with the bulk g-C<sub>3</sub>N<sub>4</sub>, which was beneficial for the reaction of H<sub>2</sub> evolution [21].

The separation efficiency of photogenerated electron-hole pairs is a

crucial factor for the photocatalytic performance. The PL spectra and time-resolved PL spectra were conducted to characterize this property. As displayed in Fig. 6a, the low PL intensity for PCNT-3 indicated the efficient electron-hole separation, the result might be caused by the N defects and fast electronic transfer on the tubular structure. Besides, the time-resolved fluorescence decay spectra were also measured and shown in Fig. 6b–d. The average life-time ( $\tau_{av}$ ) was calculated by using the following Eq. (2):

$$\tau_{av} = \frac{\sum_{i=1,2} B_i \tau_i^2}{\sum_{i=1,2} B_i \tau_i} \quad (2)$$

The calculated results showed that the  $\tau_{av}$  of bulk g-C<sub>3</sub>N<sub>4</sub>, TCN and PCNT-3 were 5.27 ns, 5.52 ns and 5.13 ns, respectively. Obviously, TCN held longer lifetime of charge carriers than bulk g-C<sub>3</sub>N<sub>4</sub>, whereas there was a decrease for PCNT-3, it could be attributed to the emergence of the band tail states, which was beneficial for the excitation of electron–hole pairs [41]. The photocurrents and electrochemical impedance spectroscopy (EIS) were conducted to learn more information about the separation and transfer of photogenerated electron-hole pairs. As displayed in Fig. 6c, PCNT-3 showed the highest photocurrent signs compared with bulk g-C<sub>3</sub>N<sub>4</sub> and TCN, indicating the best electron-hole separation efficiency and promotion of photocatalytic activity. What's more, the higher photocurrent of TCN than bulk g-C<sub>3</sub>N<sub>4</sub> also illustrated that the tubular structure was conducive to the electron-hole separation [35]. From the EIS spectra in Fig. 6d, as we know that the larger arc radius means the larger charge transfer resistance, thus the charge transfer efficiency of PCNT-3 was better than that of TCN and bulk g-C<sub>3</sub>N<sub>4</sub>. In a word, the tubular structure and P-doping were both useful methods to improve the photocatalytic activities.

Fig. 7a, b showed the photocatalytic hydrogen properties for different samples. The bulk g-C<sub>3</sub>N<sub>4</sub> prepared by traditional method performed poor hydrogen production rate of about 90  $\mu\text{mol g}^{-1} \text{h}^{-1}$ , which was 4.8 times lower than that of carbon nitride tube (430  $\mu\text{mol g}^{-1} \text{h}^{-1}$ ). Although the carbon nitride tube presented unsatisfactory light absorbance, the high surface area, tubular structure and higher efficiency of electron-hole separation made it better for photocatalytic activities than that of bulk g-C<sub>3</sub>N<sub>4</sub>. After introducing P element, the hydrogen production was obviously improved. When the mass ratio reached to the third sample, PCNT-3 yielded the highest H<sub>2</sub> evolution of 2020  $\mu\text{mol g}^{-1} \text{h}^{-1}$ , exhibiting about 4.7 folds than that of TCN and 22.4 folds of bulk g-C<sub>3</sub>N<sub>4</sub>, which was attributed to the further promotion of visible light absorbance, band structure, higher surface area, and better electron-hole separation efficiency. Meanwhile, the calculated apparent quantum efficiency (AQE) for PCNT-3 was 4.32% at 420 nm, 3.58% at 450 nm, and 1.28% at 500 nm (Fig. 7c), which was concordant with the UV–vis spectra and was higher than most of the

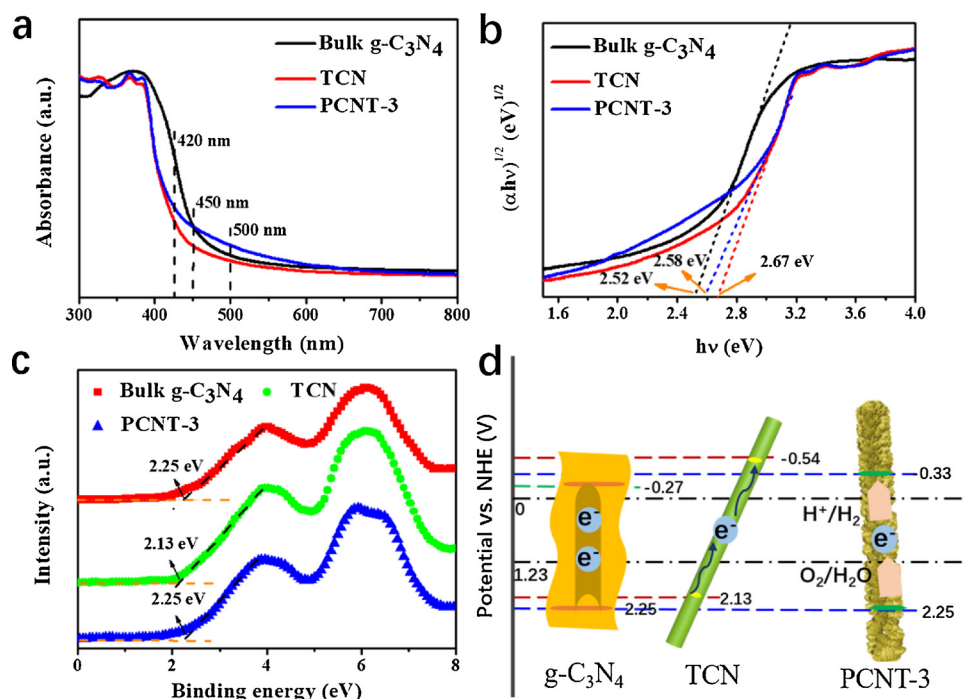


**Fig. 5.** (a) UV-vis diffuse reflectance spectra, (b) Estimated band energy spectra; (c) XPS valence band spectra, and (d) Schematic illustration of the band position for bulk  $g\text{-C}_3\text{N}_4$ , TCN and PCNT-3 samples, respectively.

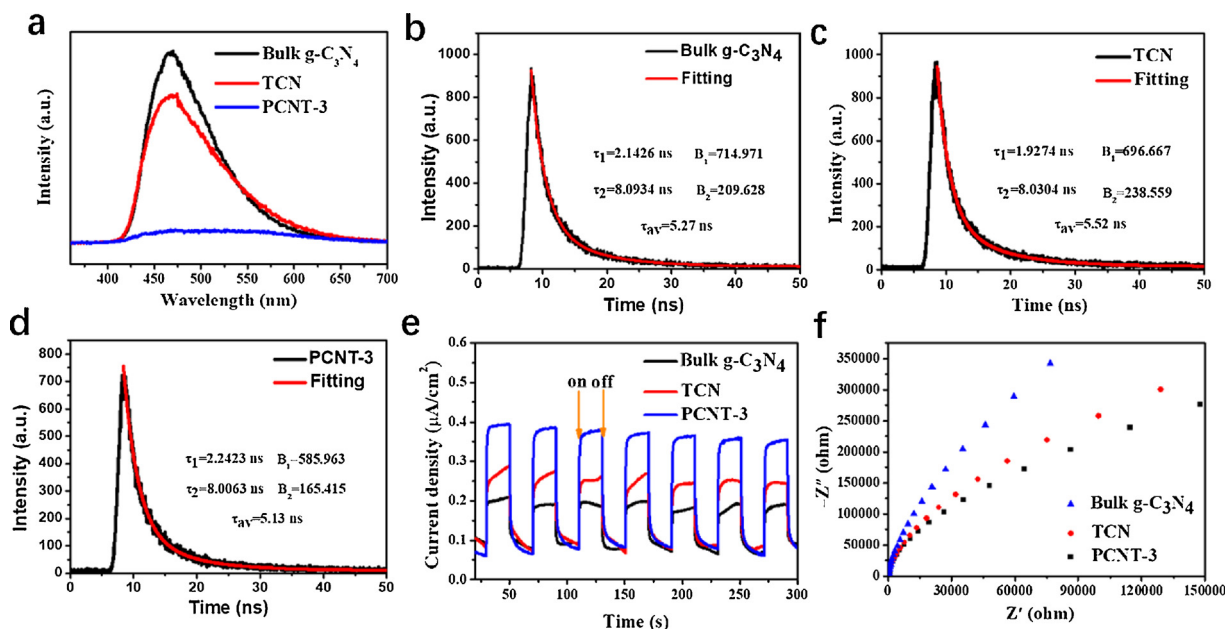


**Fig. 6.** (a) PL spectra with excitation wavelength of  $\lambda = 340$  nm, (b, c, d) Time-resolved PL spectra, (e) Photocurrent responses under visible light, (f) EIS Nyquist plots for bulk  $g\text{-C}_3\text{N}_4$ , TCN and PCNT-3 samples.

reports for P-doped carbon nitride or carbon nitride tubes (Table S3). However, further increasing phytic acid ratio would cause a decrease of  $\text{H}_2$  production, this was due to the fact that the excess amount of P dopants was considered as the recombination center to inhibit the separation of electron-hole pairs [21]. To investigate the stability of PCNT-3, the recycling test was performed for 10 h (Fig. 7d). As we can see, the  $\text{H}_2$  production rate kept almost same after 10 h reaction. Moreover, the XRD, SEM and surface areas results (Fig. S5) after recycling test showed almost no change, indicating its good durability and high stability.

On the basis of the above results and discussion for the band

structure of TCN and PCNT-x samples, a possible photocatalytic mechanism can be proposed, which is shown in Scheme 2. As the above-mentioned, the obtained photocatalysts possess the integrated merits of 1D tubular structure, 2D nanosheets and phosphorus doping. From the SEM and TEM images (Figs. 1,2), the surfaces of PCNT-x samples were made up of carbon nitride nanosheets with compact adhesion, exhibiting a tight cross-link and favorable electron transfer. Especially for the PCNT-3 sample, the flower buds-like or bubble-like structure was more profitable for the charge separation [42,43]. Besides, P-doping can extend the visible-light absorption region up to 450 nm (Fig. 5), thus PCNT-x samples can harvest the visible light to photo-excite the



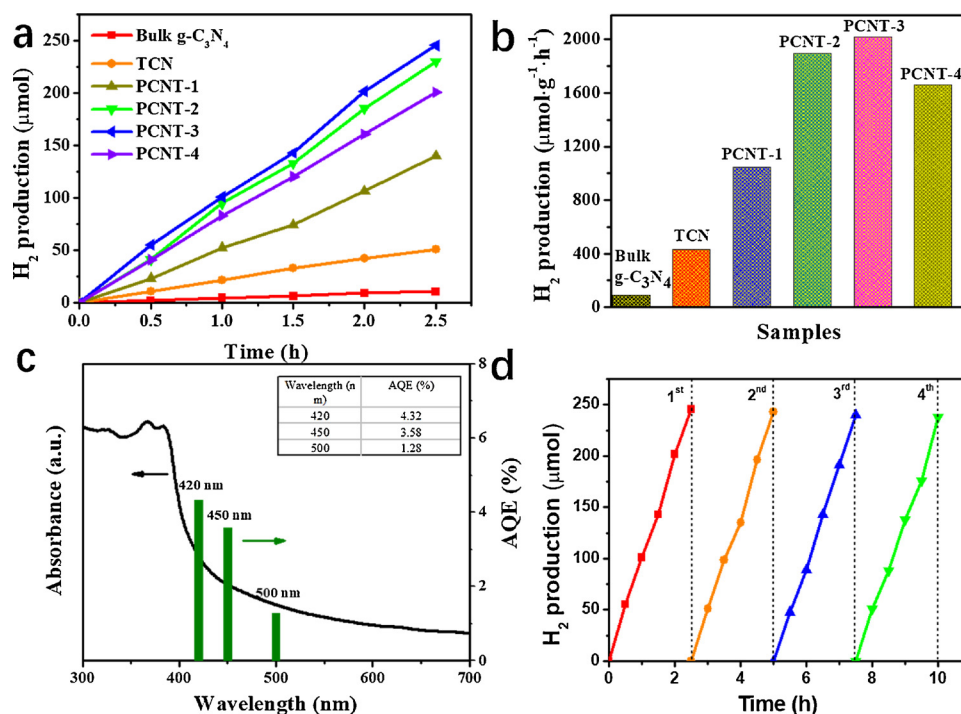
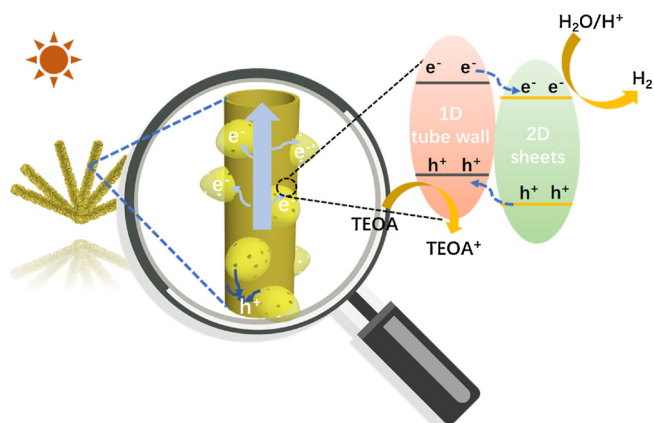


**Fig. 7.** (a) Time courses of visible-light photocatalytic H<sub>2</sub> evolution on the as-prepared photocatalyst, (b) H<sub>2</sub> production rate of bulk g-C<sub>3</sub>N<sub>4</sub>, TCN and samples with different PA ratios, (c) Wavelength-dependent AQE and DRS spectrum, (d) Cycling stability test for H<sub>2</sub> production of PCNT-3.



**Scheme 2.** Possible mechanism for the photogenerated charge transfer and induced photocatalytic H<sub>2</sub> evolution processes of PCNT.

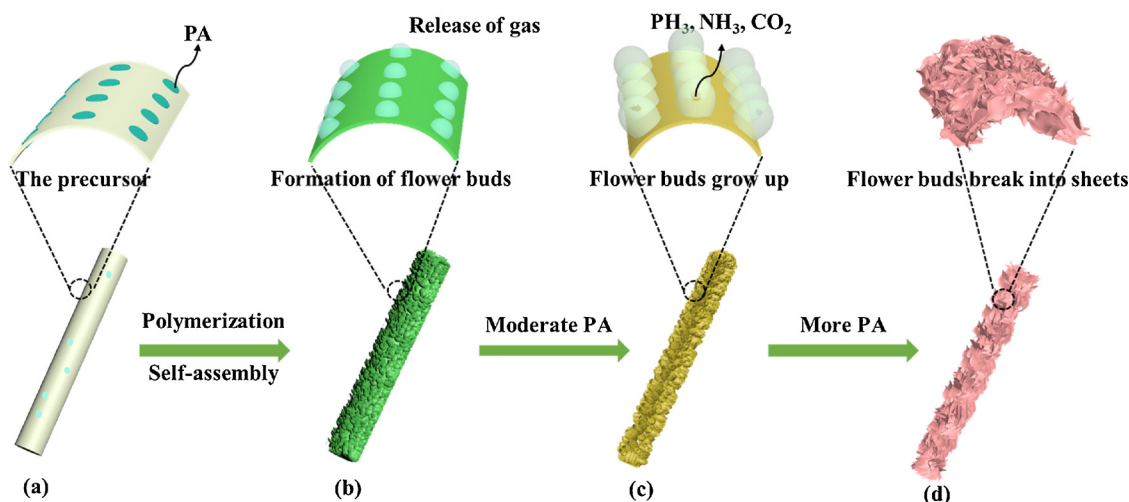
electrons to the CB and leave the photo-generated holes in the VB. As shown in Scheme 2, under the visible light excitation, the photo-excited electron-hole pairs in the interior of PCNT-*x* samples can rapidly transfer to the surface along the interlayer direction, thus the electrons can transfer from the CB of 2D nanosheets to the CB of the 1D tube, while the holes transfer from the VB of tube wall to that of the nanosheets on the surface, leading to oriented migration of electrons and holes. In addition, the fast charge transfer on the pure tube can further promote the separation efficiency along the in-plane direction. On the other hand, Pt nanoparticles, which was loaded on the surface of the photocatalysts and acted as the co-catalyst, would accumulate the photogenerated electrons to migrate from the CB for reducing H<sup>+</sup> to hydrogen, while the photogenerated holes in the reaction solution would be consumed by TEOA. Of course, the high surface area of PCNT-*x* samples also accommodates the massive absorption and catalytic-active centers and is beneficial for the rapid transfer of the reactants and products through the hierarchical structure. Therefore, the integrated combination of the above-mentioned processes would promote

the strong synergetic enhancement of the visible-light-driven photocatalytic activity.

From the above-mentioned description, it can be seen that the as-prepared g-C<sub>3</sub>N<sub>4</sub> tubes integrated the merits of 1D tube and porous P-C<sub>3</sub>N<sub>4</sub> ultrathin nanosheets, thus exhibiting a significantly improved photocatalytic hydrogen evolution performance. The morphology evolution for the g-C<sub>3</sub>N<sub>4</sub> architecture structure could be illustrated by the Scheme 3. Phytic acid played an important role in formation of porous external framework. In an aqueous solution system, HTD could easily interact with phytic acid by the involvement of heteroatom motifs [44]. Freezing drying was very crucial to form micron fibers, under the rapid cooling conduction, the ice restrained the movement of HTD molecules, resulting in making strip structure rather than traditional crystalline bulk appearance (Fig. S5), thus the fibers were obtained after the ice was removed. Without the phytic acid, carbon nitride synthesized from HTD showed a hollow tubular structure. In contrast, the addition of phytic acid made an obvious difference on the surface structure. When a quantity of phytic acid was used, the precursor was made up of two parts: one part was HTD, which only generated some common holes after pyrolysis, and the other part was phytic acid surrounded by HTD, which could create hollow flower buds on the tube surface (Scheme 3b). While there were enough phytic acid, HTD could uniformly distributed instead of reuniting, which made a possibility for more leaving space (Scheme 3c). However, if too much of phytic acid was used, the flower buds would break into sheets on the tubular structure (Scheme 3d). Furthermore, when the phytic acid was instead by phosphoric acid, the SEM images (Fig. S7) displayed a tube structure but no sheets or hollow flower buds seeded on their surface, the reason might be due to the fact that phytic acid had several phosphate groups and other organic ingredients, resulting in catching more HTD molecules and generating more release of gas, including PH<sub>3</sub>, NH<sub>3</sub>, NO, NO<sub>2</sub> and CO<sub>2</sub> [33], after the pyrolysis process.

#### 4. Conclusions

In summary, coral-like 3D porous P-doped g-C<sub>3</sub>N<sub>4</sub> tube (PCNT) photocatalysts were successfully prepared by a novel method



**Scheme 3.** Schematic illustration for the self-assembly formation of g-C<sub>3</sub>N<sub>4</sub> with different morphology and structure.

combining pyrolysis, freeze-drying and in-situ phosphorus doping. The synergistic effects of the hollow tube structure with larger specific surface area (60.57 m<sup>2</sup>/g), enhanced light absorption, as well as faster photogenerated-charge separation lead to the significantly improved photocatalytic hydrogen evolution performance. Specifically, the as-prepared PCNT exhibits an optimized hydrogen evolution rate of 2020 μmol g<sup>-1</sup> h<sup>-1</sup> and an apparent quantum efficiency of 4.32% at 420 nm, which is about 4.7 folds and 22.4 folds than that of g-C<sub>3</sub>N<sub>4</sub> tubes and pristine bulk g-C<sub>3</sub>N<sub>4</sub>, respectively. Moreover, this work highlights a new facile strategy to develop high-efficiency 1D/2D integrated g-C<sub>3</sub>N<sub>4</sub> tubes and may provide guidance for the synthesis of materials with tubular structures for solarlight-driven H<sub>2</sub> production.

### Acknowledgements

This work was financially supported by the National Natural Science Foundation of China (NSFC) Grants (51702294, 51702295) and Natural Science Foundation of Zhejiang Grants (LY18B030004). The helpful comments of three anonymous reviewers are also highly acknowledged.

### Appendix A. Supplementary data

Supplementary material related to this article can be found, in the online version, at doi:<https://doi.org/10.1016/j.apcatb.2018.09.037>.

### References

- [1] S.S. Chen, T. Takata, K. Domen, *Nat. Rev. Mater.* 2 (2017) 17050.
- [2] W.D. Liu, S.M. Xu, S.Y. Guan, R.Z. Liang, M. Wei, D.G. Evans, X. Duan, *Adv. Mater.* 30 (2018) 1704376.
- [3] Y.F. Li, R.X. Jin, Y. Xing, J.Q. Li, S.Y. Song, X.C. Liu, M. Li, R.C. Jin, *Adv. Energy Mater.* 6 (2016) 1601273.
- [4] X.C. Wang, K. Maeda, A. Thomas, K. Takanabe, G. Xin, J.M. Carlsson, K. Domen M, *Nat. Mater.* 8 (2009) 76–80.
- [5] W.J. Ong, L.L. Tan, Y.H. Ng, S.T. Yong, S.P. Chai, *Chem. Rev.* 116 (2016) 7159–7329.
- [6] L.F. Cui, J.L. Song, A.F. McGuire, S.F. Kang, X.Y. Fang, J.J. Wang, C.C. Yin, X. Li, Y.G. Wang, B.X. Cui, *ACS Nano* 12 (2018) 5551–5558.
- [7] J. Liu, Y. Liu, N.Y. Liu, Y.Z. Han, X. Zhang, H. Huang, Y. Lifshitz, S.T. Lee, J. Zhong, Z.H. Kang, *Science* 347 (2015) 970–974.
- [8] P.F. Xia, M.J. Liu, B. Cheng, J.G. Yu, L.Y. Zhang, *ACS Sustain. Chem. Eng.* 6 (2018) 8945–8953.
- [9] J. Xu, Z.P. Wang, Y.F. Zhu, *ACS Appl. Mater. Interfaces* 9 (2017) 27727–27735.
- [10] C.Z. Sun, H. Zhang, H. Liu, X.X. Zheng, W.X. Zou, L. Dong, L. Qi, *Appl. Catal. B: Environ.* 235 (2018) 66–74.
- [11] L.B. Jiang, X.Z. Yuan, G.M. Zeng, X.H. Chen, Z.B. Wu, J. Liang, J. Zhang, H. Wang, H. Wang, *ACS Sustain. Chem. Eng.* 5 (2017) 5831–5841.
- [12] L.F. Gao, T. Wen, J.Y. Xu, X.P. Zhai, M. Zhao, G.W. Hu, P. Chen, Q. Wang, H.L. Zhang, *ACS Appl. Mater. Interfaces* 8 (2016) 617–624.
- [13] L.X. Wang, Y. Li, X.C. Yin, Y.Z. Wang, A.L. Song, Z.P. Ma, X.J. Qin, G.J. Shao, *ACS Sustain. Chem. Eng.* 5 (2017) 7993–8003.
- [14] R.A. Rather, S. Singh, B. Pal, *Appl. Catal. B: Environ.* 213 (2017) 9–17.
- [15] H. Park, J.H. Lee, E.H. Kim, K.Y. Kim, Y.H. Choi, D.H. Youn, J.S. Lee, *Chem. Commun.* 52 (2016) 14302–14305.
- [16] H. Pan, Y.W. Zhang, V.B. Shenoy, H.J. Gao, *ACS Catal.* 1 (2011) 99–104.
- [17] M. Wu, J. Zhang, C.X. Liu, Y.S. Gong, R. Wang, B.B. He, H.W. Wang, *ChemCatChem* 10 (2018) 3069–3077.
- [18] Y.G. Tan, Z. Shu, J. Zhou, T.T. Li, W.B. Wang, Z.L. Zhao, *Appl. Catal. B: Environ.* 230 (2018) 260–268.
- [19] C. Wang, H.Q. Fan, X.H. Ren, J.W. Ma, J.W. Fang, W.J. Wang, *ChemSusChem* 11 (2018) 700–708.
- [20] Q. Han, B. Wang, J. Gao, Z.H. Cheng, Y. Zhao, Z.P. Zhang, L.T. Qu, *ACS Nano* 10 (2016) 2745–2751.
- [21] H.B. Fang, X.H. Zhang, J.J. Wu, N. Li, Y.Z. Zheng, X. Tao, *Appl. Catal. B: Environ.* 225 (2018) 397–405.
- [22] Y.C. Deng, L. Tang, G.M. Zeng, Z.J. Zhu, M. Yan, Y.Y. Zhou, J.J. Wang, Y.N. Liu, J.J. Wang, *Appl. Catal. B: Environ.* 203 (2017) 343–354.
- [23] G. Zhao, Y.L. Cheng, Y.Z. Wu, X.J. Xu, X.P. Hao, *Small* 14 (2018) 1704138.
- [24] J.J. Wu, N. Li, X.H. Zhang, H.B. Fang, Y.Z. Zheng, X. Tao, *Appl. Catal. B: Environ.* 226 (2018) 61–70.
- [25] Z. Chen, X. Yu, Q.H. Zhu, T.T. Fan, Q.L. Wu, L.Z. Zhang, J.H. Li, W.P. Fang, X.D. Yi, *Carbon* 139 (2018) 189–194.
- [26] H. Wang, B. Wang, Y. Bian, L.M. Dai, *ACS Appl. Mater. Interfaces* 9 (2017) 21730–21737.
- [27] Z.X. Zeng, K.X. Li, L.S. Yan, Y.H. Dai, H.Q. Guo, M.X. Huo, Y.H. Guo, *RSC Adv.* 4 (2014) 59513–59518.
- [28] K. Li, X. Xie, W.D. Zhang, *ChemCatChem* 8 (2016) 2128–2135.
- [29] M. Shalom, M. Guttentag, C. Fettkenhauer, S. Inal, D. Neher, A. Llobet, M. Antonietti, *Chem. Mater.* 26 (2014) 5812–5818.
- [30] Z.J. Huang, F.W. Yan, G.Q. Yuan, *ACS Sustain. Chem. Eng.* 6 (2018) 3187–3195.
- [31] Z.W. Tong, D. Yang, Y.Y. Sun, Y.H. Nan, Z.Y. Jiang, *Small* 10 (2016) 4093–4101.
- [32] G.G. Zhang, A. Savateev, Y.B. Zhao, L.N. Li, M. Antonietti, *J. Mater. Chem. A* 5 (2017) 12723–12728.
- [33] S.E. Guo, Z.P. Deng, M.X. Li, B.J. Jiang, C.G. Tian, Q.J. Pan, H.G. Fu, *Angew. Chem. Int. Ed.* 55 (2016) 1830–1834.
- [34] B. Liu, L.Q. Ye, R. Wang, J.F. Yang, Y.X. Zhang, R. Guan, L.H. Tian, X.B. Chen, *ACS Appl. Mater. Interfaces* 10 (2018) 4001–4009.
- [35] Z. Mo, H. Xu, Z.G. Chen, X.J. She, Y.H. Song, P.C. Yan, L. Xu, Y.C. Lei, S.Q. Yuan, H.M. Li, *Appl. Catal. B: Environ.* 225 (2018) 154–161.
- [36] J.R. Ran, T.Y. Ma, G.P. Gao, X.W. Du, S.Z. Qiao, *Energy Environ. Sci.* 8 (2015) 3708–3717.
- [37] X.G. Ma, Y.H. Lv, J. Xu, Y.F. Liu, R.Q. Zhang, Y.F. Zhu, *J. Phys. Chem. C* 116 (2012) 23485–23493.
- [38] S.E. Guo, Y.Q. Tang, Y. Xie, C.G. Tian, Q.M. Feng, W. Zhou, B.J. Jiang, *Appl. Catal. B: Environ.* 218 (2017) 664–671.
- [39] Y.Z. Hong, C.S. Li, D. Li, Z.Y. Fang, B.F. Luo, X. Yan, H.Q. Shen, B.D. Mao, W.D. Shi, *Nanoscale* 9 (2017) 14103–14110.
- [40] L. Sun, W. Hong, J. Liu, M.J. Yang, W.S. Lin, G.J. Chen, D.S. Yu, X.D. Chen, *ACS Appl. Mater. Interfaces* 9 (2017) 44503–44511.
- [41] Q. Han, Z.H. Cheng, B. Wang, H.M. Zhang, L.T. Qu, *ACS Nano* 12 (2018) 5221–5227.
- [42] P.Y. Wang, C.S. Guo, S. Hou, X. Zhao, L.L. Wu, Y.Y. Pei, Y. Zhang, J.F. Gao, J. Xu, J. Alloys Compd. 769 (2018) 503–511.
- [43] Q.Y. Guo, Y.H. Zhang, H.S. Zhang, Y.J. Liu, Y.J. Zhao, J.R. Qiu, G.P. Dong, *Adv. Funct. Mater.* 27 (2017) 1703711.
- [44] T.Y. Ma, J.R. Ran, S. Dai, M. Jaroniec, S.Z. Qiao, *Angew. Chem. Int. Ed.* 54 (2015) 4646–4650.